Cascading Constraints from Neutrino Emitting Blazars: The case of TXS 0506+056

Anita Reimer,¹ Markus Böttcher,² and Sara Buson³

¹ Institute for Astro- & Particle Physics, University of Innsbruck, 6020 Innsbruck, Austria
² Centre for Space Research, North-West University, Potchefstroom, 2531, South Africa
³ NASA Postdoctoral Program Fellow, Universities Space Research Association, USA
based at NASA Goddard Space Flight Center, Greenbelt, MD 20771, USA
now at University of Würzburg, 97074 Würzburg, Germany

(Accepted June 22, 2019)

ABSTRACT

We present a procedure to generally constrain the environments of neutrino-producing sites in photomeson production models of jetted Active Galactic Nuclei (AGN) where any origin of the dominant target photon field can be accommodated. For this purpose we reconstruct the minimum target photon spectrum required to produce the (observed) neutrino spectrum, and derive the distributions of all corresponding secondary particles. These initiate electromagnetic cascades with an efficiency that is linked to the neutrino production rate. The derived photon spectra represent the minimum radiation emerging from the source that is strictly associated with the photo-hadronically produced neutrinos.

Using the 2014–15 neutrino spectrum observed by IceCube from TXS 0506+056, we conduct a comprehensive study of these cascade spectra and compare them to the simultaneous multi-wavelength emission. For this set of observations, photopion production from a co-spatially produced (co-moving) photon target can be ruled out as well as a setup where synchrotron or Compton-synchrotron supported cascades on a stationary (AGN rest frame) target photon field operate in this source. However, a scenario where Compton-driven cascades develop in the stationary soft-X-ray photon target which photo-hadronically produced the observed neutrinos appears feasible with required proton kinetic jet powers near the Eddington limit. The source is then found to produce neutrinos inefficiently, and emits GeV photons significantly below the observed Fermi-LAT-flux. Hence, the neutrinos and the bulk of the gamma rays observed in 2014/2015 from TXS 0506+056 cannot have been initiated by the same process.

Keywords: galaxies: active — galaxies: jets — gamma-rays: galaxies — radiation mechanisms: non-thermal — relativistic processes — neutrinos

1. INTRODUCTION

Active Galactic Nuclei (AGN) have long been considered to be among the source populations responsible for the ultra-high energy cosmic rays observed at Earth. Indeed, members of this source population fulfill the Hillas criterion (Hillas 1984) as well as energetics requirements to accelerate charged particles to such extreme energies, in principle. These relativistic hadrons interact in the highly radiative environment of AGN, if above the threshold for photomeson

and/or Bethe-Heitler pair production, or interact in dense material associated with the AGN via inelastic nucleon-nucleon interactions, to produce secondary particles, among them electron-positron pairs, neutrinos and high-energy photons. Hence, for just as long, gamma-ray loud AGN have been predicted as sources of neutrinos (Mannheim & Biermann 1989; Stecker et al. Mannheim et al. 1992: Protheroe & Szabo 1992; Mannheim 1993; Szabo & Protheroe 1994; Mastichiadis 1996; Bednarek & Protheroe 1997, 1999; Protheroe 1999; Mücke & Protheroe 2001; Mannheim et al. 2001; Atoyan & Dermer 2001; Protheroe et al. 2003; Atoyan & Dermer 2001; Mücke et al. 2003; Reimer et al. 2004; Dermer et al. 2009; Dimitrakoudis et al. 2012;

Dermer et al. 2012; Böttcher et al. 2013; Halzen 2013; Murase et al. 2014; Dermer et al. 2014; Gao, S. et al. 2017; Murase et al. 2018).

Until a few years ago, multi-messenger astrophysics was merely a prediction by (some) cosmic-ray the-It turned into reality with the first detections of high-energy neutrinos of astrophysical origin (Aartsen et al. 2013). Observationally, no individual sources could be associated with these neutrino events, which were found to be isotropically distributed over the sky (Aartsen et al. 2014). Most interestingly, the total diffuse flux of these neutrinos follows a differential spectrum not harder than $dN/dE \propto E^{-2}$ above a few tens of TeV and ranging to almost 10 PeV (Aartsen et al. 2015). The detection of these neutrinos initiated an avalanche of hadronic emission models for various possible high-energy source populations, among them blazars, a sub-class of jetted AGN with the line-of-sight close to the jet axis. are the most numerous sources in the extragalactic GeV-TeV γ -ray sky (e.g., Reimer & Böttcher 2013; Acero et al. 2015; Ackermann et al. 2016). The fact that in hadronic interactions, roughly equal powers of high-energy photons + pairs and neutrinos are produced (e.g., Mannheim & Schlickeiser 1994; Mücke et al. 2000) makes these γ -ray blazars plausible sources of the detected neutrinos (e.g., Dimitrakoudis et al. 2014; Krauss et al. 2014; Cerruti et al. 2015; Padovani et al. 2015; Petropoulou et al. 2015; Kadler et al. One-zone blazar emission models, where neutrinos are produced in photo-hadronic interactions, typically predict neutrino spectra peaking at or beyond PeVenergies, with extremely hard spectral shapes below (e.g., Mücke et al. 2003; Dermer et al. 2012) when applied to GeV γ -ray sources.

Recently, neutrino astrophysics experienced a further boost when the BL Lac object TXS 0506+056 was found within the 50 % containment region of the single IceCube event IceCube-EHE-170922A (Aartsen et al. 2018a), and simultaneously in an elevated flux state in the Fermi-LAT energy range (Aartsen et al. 2018a) at the time this event was detected. Furthermore, an extended neutrino excess (designated the "neutrino flare" in the following) consisting of ~ 13 neutrino events detected in a $110\pm_{24}^{35}$ days period in September 2014 - March 2015 was found from the same source (Aartsen et al. 2018b). This has motivated the suggestion that TXS 0506+056 is the source of these detected neutrinos (Aartsen et al. 2018a), implicitly assuming a causal connection between the neutrino and γ -ray emission. Such a link is justified if at least part of these ≥ GeV-photons have been initiated by the same process

responsible for the neutrino flux, or have at least been produced in the same emission region of the source¹. It is, however, questionable whether a \geq GeV γ -ray emitting source can simultaneously be an efficient producer of neutrinos in the 10 - 100 TeV energy range, in the framework of a photo-hadronic emission model (e.g., Begelman et al. 1990). The latter requires a photomeson production optical depth $\tau_{p\gamma} \gg 1$ in a field of target photons at UV-to-X-ray energies (see Sect. 3.1), while the former requires GeV-photons to escape the source, hence the $\gamma\gamma$ -pair production optical depth $\tau_{\gamma\gamma} \ll 1$ for target photons at X-ray energies. Hence, the same target radiation field necessary for neutrino production is also a source of opacity for \geq GeV photons. Observe that a ratio of $\tau_{p\gamma}/\tau_{\gamma\gamma} \gg 1$ is required in order for the radiation to escape, while $\tau_{p\gamma}/\tau_{\gamma\gamma} \approx \sigma_{p\gamma}/\sigma_{\gamma\gamma} \ll 1$ is guaranteed by the nature of the processes.

In this work we present a procedure that provides, in the framework of photo-hadronically produced neutrinos in jetted AGN, constraints on their associated broadband photon spectral energy distribution (SED) in a way that is independent of the origin of the dominant target photon field. It is expected to guide searches for neutrino source associations with electromagnetic counterparts for cases of highly radiative sources where neutrinos are produced predominantly photo-hadronically. We present this procedure by applying it to the 2014 – 15 neutrino flare of TXS 0506+056. The resulting constraints are then discussed to infer limits on the required source power and multi-wavelength (MWL) predictions of the photon SED. The comparison to MWL data allows us in turn to constrain models.

In the following, we first (Sect. 2) present the quasisimultaneous multi-messenger data acquired for the time period of the 2014 - 15 neutrino flare, to be placed into a generic theoretical set-up where neutrinos are produced photo-hadronically in a relativistic jet. The subsequent Section 3 describes the simulations of electromagnetic cascades initiated by photo-hadronic processes and the constraints that can be deduced from them. Section 4 then discusses implications for the nature of the target photon field for photo-hadronic processes responsible for the neutrino emission, where we will show that the only plausible scenario of photo-pion production in the jet of TXS 0506+056 requires a stationary UV - X-ray target photon field external to the jet that leads to Comptonsupported photo-pion-induced cascades. We find that in this set-up the neutrino-production optical depth is

 $^{^{\}rm 1}$ In this case co-acceleration of electrons and protons can be expected to provide a causal connection between photon and neutrino production.

surprisingly low during the neutrino flare unlike the case of efficient neutrino production, $\tau_{p\gamma}\gg 1$. This in turn allows photon escape of any origin from the neutrino production site only below $\sim 10^{-5}E_{\nu,\rm obs}$ (with $E_{\nu,\rm obs}$ the observed neutrino energy). The γ -ray flux strictly associated with the neutrino flare is shown to lie significantly below the GeV-flux detected contemporaneous with the IceCube neutrino flare, implying no common production origin between the observed IceCube neutrinos and LAT gamma rays. In Section 5 we provide a summary of our results and conclusions. Throughout the paper, primed quantities refer to the co-moving jet frame of the emission region. Physical quantities are parameterized as $Q=10^i\,Q_i$ in c.g.s units.

2. QUASI-SIMULTANEUOUS MULTI-MESSENGER DATA OF THE JET

2.1. Neutrino data

The neutrino flux from the 2014 – 15 neutrino flare of TXS 0506+056 was best described by a spectrum between 32 TeV and 3.6 PeV of the form $\Phi_{\nu}(E_{\nu})=\Phi_0\,E_{14}^{-2.1}$ with $\Phi_0=2.2\times10^{-15}~{\rm cm}^{-2}~{\rm s}^{-1}$ TeV⁻¹ and $E_{14}\equiv E_{\nu}/(100\,{\rm TeV})$ (Aartsen et al. 2018b). For a redshift of TXS 0506+056 as measured by Ajello et al. (2014) and Paiano et al. (2018), z=0.3365, which corresponds to a luminosity distance of $d_L\approx1.8~{\rm Gpc}\approx5.5\times10^{27}$ cm, the IceCube neutrino flux corresponds to an isotropic-equivalent luminosity in muon neutrinos of $L_{\nu,{\rm iso}}\approx5.8\times10^{46}~{\rm erg~s}^{-1}$.

We assume that the neutrinos are produced by relativistic hadrons in the high-energy emission region (sometimes referred to as the 'blob') of (jet-frame) size R', moving relativistically along the jet with constant Lorentz factor $\Gamma \equiv 10\,\Gamma_{10}$ and viewing angle $\theta_{\rm obs}$, resulting in relativistic Doppler boosting by the Doppler factor $D = (\Gamma \left[1 - \beta_{\Gamma} \cos \theta_{\rm obs}\right])^{-1} \equiv 10\,D_1$ with $\beta_{\Gamma}c$ the bulk velocity. In that case, the total neutrino luminosity (comprising all neutrino flavors and assuming complete flavor mixing) produced in the co-moving frame of the emission region is reduced to $L'_{\nu} \approx 1.7 \times 10^{43}\,D_1^{-4}~{\rm erg~s^{-1}}$.

2.2. Photon data

To study the electromagnetic behaviour of TXS 0506+056 during the neutrino flare we collect data in the optical, X-rays and γ -ray bands. Optical V-band and g-band data are obtained from the All-Sky Automated Survey for Supernovae (Shappee et al. 2014; Kochanek et al. 2017). Data are publicly available from the ASAS-SN website² and available between 2014 February 2 – 2018

September 25. At X-ray energies, we use data from the Burst Alert Telescope (BAT), on board the Neil Gehrels Swift Observatory, to derive a constraint at keV energies for a time interval simultaneous with the neutrino flare. The Fermi-Large Area Telescope (LAT) has been monitoring the whole sky for almost ten years, including the relevant period of the neutrino flare as described in 2.2.2.

2.2.1. Swift-BAT data analysis

The BAT survey data were retrieved from the HEASARC public archive³ and processed using the BATIMAGER code (Segreto et al. 2010), dedicated to the processing of coded mask instrument data, that performs processing and cleaning of the data, source detection, and production of background subtracted images and other scientific products. TXS 0506+056 is not detected in the whole set of survey data, spanning from December 2004 to November 2017. Using the 20-85 keV sensitivity map, for the time period spanning September 16, 2014 to February 28, 2017 we have derived an upper limit of $9.12 \cdot 10^{-12}$ erg cm⁻² s⁻¹ to its flux, at a 5σ level.

2.2.2. Fermi-LAT data

In this work we consider ten years of Fermi-LAT data, collected between 2008 August 4 and 2018 September 29 (MJD 54682-58390). Events are selected in a $10^{\circ} \times 10^{\circ}$ square centered on the position of TXS 0506+056, from 100 MeV up to 300 GeV. To minimize the contamination from γ rays produced in the Earth's atmosphere, we apply a zenith angle cut of $\theta < 90^{\circ}$. Time periods during which the LAT has detected bright solar flares and γ -ray bursts were excluded. We perform a binned likelihood analysis with the package fermipy⁴ (v0.17.3), based on the standard LAT ScienceTools⁵ (v11-07-00) and the P8R2_SOURCE_V6 instrument response functions. The model of the region accounts for all sources included in the Fermi-LAT preliminary 8-year source list⁶, and contained in a 15° region from the position of TXS 0506+056, as well as the isotropic and Galactic diffuse γ -ray emission models (iso_P8R2_SOURCE V6 v06.txt and gll_iem_v06.fits). The spectral parameters of the bright γ -ray object located 1.2° from TXS 0506+056 and associated with the blazar PKS 0502+049, are left free to vary in the fit. Similarly to Garrappa et al.

² https://asas-sn.osu.edu/

³ http://heasarc.gsfc.nasa.gov/docs/archive.html

⁴ https://fermipy.readthedocs.io

⁵ http://fermi.gsfc.nasa.gov/ssc/data/analysis/

⁶ FL8Y preliminary catalog: https://fermi.gsfc.nasa.gov/ssc/data/access/lat/fl8y/

(in prep.), the residual map of the region does not show evidence for significant structures, indicating that our best-fit model adequately describes the region.

To investigate the γ -ray data of TXS 0506+056 during the neutrino flare, we adopt as definition for the time interval the "box window" identified by Aartsen et al. (2018b), i.e. 158 days (MJD 56937 to MJD 57096, that is 2014-10-07 to 2015-03-15). For this period, the γ -ray SED of TXS 0506+056 is well modelled with a power-law spectral shape. A maximum likelihood fit yields the best-fit (> 100 MeV) flux value of $(3.3\pm0.9)\cdot10^{-8} {\rm cm}^{-2} {\rm s}^{-1}$, with a photon spectral index of 1.9 ± 0.1 , and the source is detected at a significance of more than 12σ . This gives an isotropic equivalent gamma-ray luminosity in the LAT-energy range during the neutrino flare of $1.9\cdot10^{45} {\rm erg~s}^{-1}$, or $1.9\cdot10^{41}D_1^{-4} {\rm erg~s}^{-1}$ in the co-moving frame of the jet.

Downturns or upturns in the MeV-GeV spectrum of TXS 0506+056 could be interesting to confirm / rule out features generated by the cascade scenarios. A previous work reported a hint for a hardening of the TXS 0506+056 spectrum in the > 2 GeV LAT band (Padovani et al. 2018) during the 2014-15 "neutrino flare" interval. Issues arising from source confusion at the lower LAT energies prevented the same authors from conducting a full investigation of the blazar spectrum in the >100 MeV range. In our analysis we are able to overcome these issues by accounting for the nearby known bright gamma-ray blazar PKS 0502+049 in our model for the region of interest, and allowing its spectral parameters to vary in the fit. During the neutrino flare, we find that the source flux is consistent with a quiescent state and the spectral shape with the average one in the > 100 MeV range (see also Garrappa et al. in prep.). Including this full broad-band information provided by the LAT allows us to rule out a large variety of cascade scenarios, as explained in more detail in Sec. 3.2.

Fig. 1 shows the γ -ray and optical light curves. The Fermi-LAT light curve is computed with an 8-weeks binning, integrating energies above 300 MeV. The time bin edges are chosen to conveniently overlap with the neutrino flare, highlighted by the green shaded area in 1. Notably, the detection of the high-energy neutrino IC170922A (red line) coincides with the major γ -ray outburst experienced by TXS 0506+056 in the ten years of γ -ray monitoring, reaching a peak flux of $(1.20\pm0.07)\cdot10^{-7} {\rm cm}^{-2} {\rm s}^{-1}$. The more recent 2018 data highlight the fading trend of the flare, while the flux remains still at higher-than-average values. The behaviour in the optical band overall matches quite well the major γ -ray variations, displaying a lower-than average optical flux during times coincident with the neutrino flare.

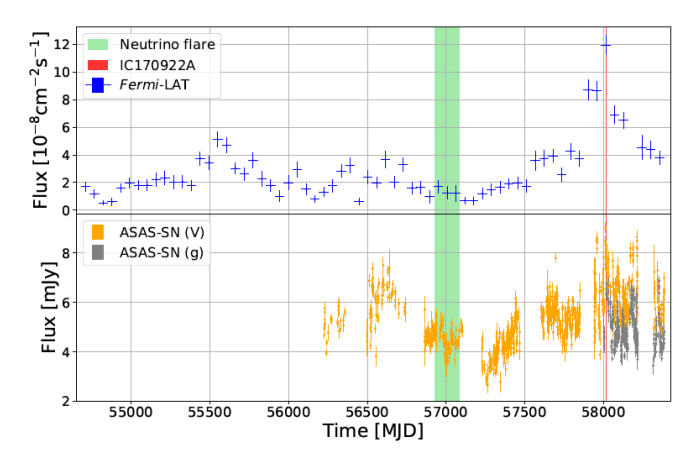


Figure 1. Top: Fermi-LAT light curve (photon flux integrated above 300 MeV) of TXS 0506+056 since mission start using 8-weeks binning. Bottom: Optical light curve from ASAS-SN in the V (yellow) and γ -ray (gray) bands. The green shaded area indicates the time interval of the neutrino flare while the red line corresponds to the detection time of the IceCube-EHE-170922A event.

The brightest prolonged variations are coincident with the major γ -ray flare and IC170922A.

3. THEORETICAL SETUP

The following section is devoted to deriving the minimal requirements on the target photon field and the relativistic proton population to explain the observed neutrino (flare) flux and spectrum in a way that is as independent of model assumptions as is possible. We will then discuss implications for the environment where the neutrino production occurs. The focus lies on the region where the neutrino production takes place. Our proposed procedure as illustrated by the flow chart in Fig. 2 does not require a full multi-messenger modelling, but nevertheless will be able to constrain the family of emission models by comparing with MWL data.

In our minimal setup we consider all neutrinos to be produced photo-hadronically in the jet of TXS 0506+056. The calculations of all particle-photon and photonphoton interactions are carried out in the jet-frame, where we assume, for simplicity, the target radiation field to be isotropic. For external target radiation fields the angular distribution of the target photons in the co-moving jet frame may become anisotropic and will lead to an increase or lowering of the particle-photon and photon-photon collision rate by an amount that depends essentially on the relative location of the emission region with respect to the source of the target photons (e.g., Protheroe, Mastichiadis & Dermer 1992; Dermer & Schlickeiser 1993; Roustazadeh & Böttcher 2010; Sitarek & Bednarek 2012; Dermer et al. 2012). We expect only minor changes of the correspond-

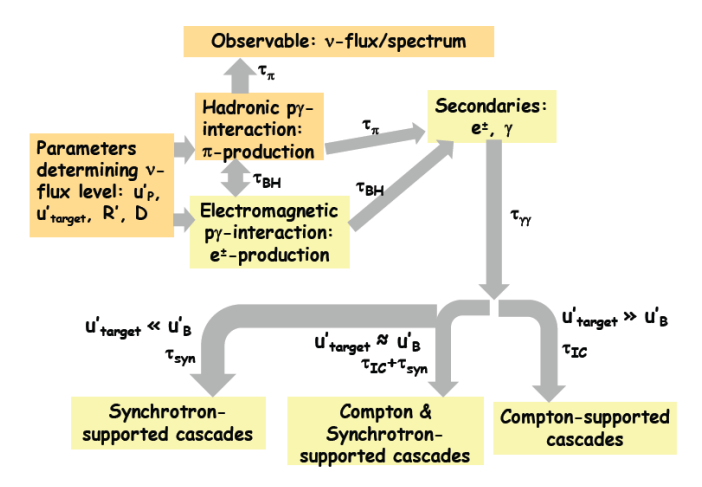


Figure 2. Flow chart of our theoretical scheme. A fit to the IceCube neutrino spectrum during the 2014 – 2015 neutrino flare determines a combination of parameters pertaining to the relativistic proton spectrum and the target photon field, leaving their relative normalization as a free parameter. A specific choice of proton power (and, thus, target photon energy density) determines the $\gamma\gamma$ opacity of the region. Depending on the relative energy densities of the magnetic field and the target photon fields, electromagnetic cascades develop in the synchrotron-, synchrotron-Compton, or Compton-dominated regimes.

ing photon emission for this case as discussed below (Sect. 3.2). A quantitative comprehensive study of general anisotropy effects for the present setup is in progress and will be presented in a forthcoming work (Reimer et al., in prep.). The resulting yields are then transformed into the observer frame. The secondary particles from particle-photon interactions initiate pair cascades in the emission region which we follow to calculate the emerging photon SED. The pair cascading is considered to be linear i.e., the pair compactness is modest or low: $L'_i\sigma_T/(R'm_ec^3) < 10$, where L'_i is the injected particle power, σ_T the Thomson cross section, and R' the size of the emission region (Svensson 1987), and the calculations consider the steady-state case.

3.1. Proton-photon interactions and neutrino production

Neutrinos are produced through hadronic interactions of relativistic protons of (jet-frame) energy $E_p' = \gamma_p' m_p c^2$ with target photons of (jet-frame) energy ϵ' when the center-of-momentum frame energy \sqrt{s} of the interaction is above threshold, i.e., $\sqrt{s} > \sqrt{s_{\rm thr}} = (m_p + m_\pi)c^2 \simeq 1.08$ GeV. The nucleon energy required to produce neutrinos at hundreds of TeV energies, $E_\nu \equiv 100 \, E_{14}$ TeV is $E_p' \simeq 200 E_{14}/(D_1 \xi_{0.05})$ TeV (i.e., $\gamma_p' = E_p'/m_p c^2 \simeq 2 \times 10^5 E_{14}/(D_1 \xi_{0.05})$) where $\xi \equiv 0.05 \, \xi_{0.05}$ is the average neutrino energy per injected nucleon energy in photo-hadronic interactions

(Mücke et al. 1999). Protons of this energy are very inefficiently emitting synchrotron radiation in the magnetic fields typically assumed in hadronic blazar models ($B \sim 10-100~\rm G$) with observed synchrotron cooling time scales of $t_{\rm psy}^{\rm obs} \sim 25\,D_1^{-1}\,B_1^{-2}\,(\gamma/[6\times10^6])^{-1}\,\rm yr,$ where $B_1 \equiv B/(10~\rm G)$. The Larmor radius of protons with such energy is $r_L \sim 2\times10^{12}\,(\gamma/[6\times10^6])\,B_1^{-1}$ cm, indicating that they are expected to be well confined within the emission region and can plausibly be accelerated by standard mechanisms, such as Diffusive Shock Acceleration.

With the threshold condition, $\epsilon' E'_p \geq 0.14 \text{ GeV}^2$, one finds the minimum energy of the target photons required to produce neutrinos at tens of TeV energies, $\epsilon' >$ $0.7D_1\xi_{0.05}/E_{14}$ keV. For pion (and neutrino) production at the Δ^+ resonance, where $s = D_{\Delta^+}^2 = (1232 \,\text{MeV})^2$, target photons of $\epsilon' \geq 1.6D_1\xi_{0.05}/E_{14}$ keV are required. In order to produce neutrinos in a broad spectral range we consider the injection of relativistic protons with a power-law distribution $dN_p'/dE_p' \propto E_p^{'-\alpha_p}$ in the range $E_p' = [m_p c^2, E_{p,\text{max}}']$ in a target photon field of photon energy density u_t' , and use the SOPHIA Monte Carlo code (Mücke et al. 2000) to calculate all resulting yields. We parametrize the target field using a simple power law for its differential photon spectrum $n_t' \propto \epsilon'^{-\alpha_t}$ in the energy range $\epsilon' = [\epsilon'_{\min}, \epsilon'_{\max}]$ and re-construct (using the SOPHIA code) the minimal target photon field, irrespective of its origin, that is required to explain the observed neutrino spectrum upon injection of a power-law proton distribution. ⁷

Fig. 3 shows the resulting muon neutrino (dotted and dashed-triple-dotted black lines) and electron neutrino (dashed and dashed-dotted black lines) spectra at production for a 'blob' that is moving with D=10. The spectra are produced assuming that protons with a power-law spectrum with index $\alpha_p=2$ and energies up to $E'_{p,\text{max}}=30$ PeV interact with a distribution of target photons with spectral index $\alpha_t=1$, between energies $\epsilon'_{\text{min}}=10$ keV and $\epsilon'_{\text{max}}=60$ keV. Neutrondecay neutrinos would appear at $\sim 10^{-3}$ smaller energies, and are not considered here. We adopted somewhat higher target photon energies than naively estimated so that the simulated neutrino spectrum matches the best-fit spectrum for the 2014/15 neutrino flare reported by the IceCube collaboration. Looking at the

⁷ The minimal target photon field is the narrowest possible soft photon spectrum with a shape and normalization that yields the observed neutrino spectrum upon injection of a power-law distribution of protons interacting photohadronically with these soft photons. The required normalization depends strongly on the proton distribution, unlike the photon spectral shape for sufficiently narrow target field spectra.

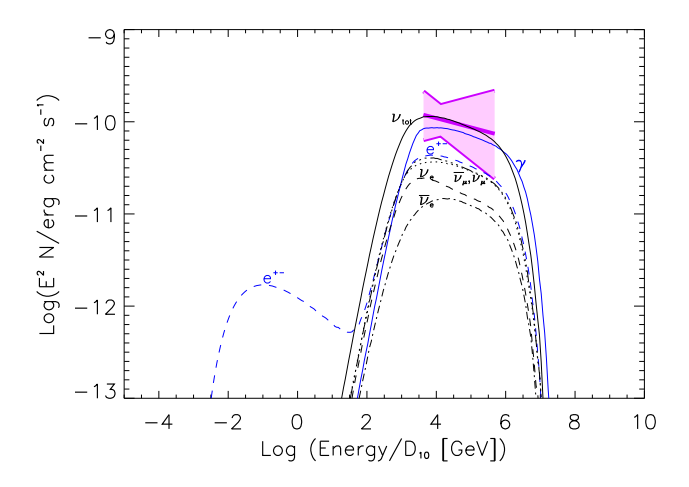


Figure 3. Secondary particles (muon neutrinos: dotted black lines, anti-muon neutrinos: dashed-triple dotted black lines, electron neutrinos: dashed black lines, anti-electron neutrinos: dashed-dotted black lines, total neutrino yield: solid black line, electron-positrons: dashed blue line, photons: solid blue line) at production due to proton-photon interactions (photo-meson and Bethe-Heitler pair production) on the same target photon field, in comparison to the total flux as measured by IceCube during the 2014 – 15 neutrino flare (violet bow tie), corrected for neutrino oscillations. Energies and fluxes are given in the observer frame.

SED of TXS 0506+056, the required energy of the target photon field coincides with the rising part of the second, high-energy hump, where the electromagnetic spectrum follows roughly $dN/dE \propto E^{-1}$. This motivates the choice of $\alpha_t = 1$. The observational uncertainties of the neutrino spectrum are well captured by varying the proton spectral index, in the range $\alpha_p = 2.0 \pm_{0.2}^{0.1}$ along with a corresponding proton spectrum normalization variation by $\pm 10\%$ (see Fig. 4). The calculation of the total neutrino spectrum (black solid lines in Fig. 3 & 4) takes into account neutrino oscillations, and is compared to the IceCube observations (violet bow tie) of the neutrino flare. Once the target photon spectral shape and Doppler factor are fixed, the neutrino flux normalization depends further on the injected proton energy density u'_{p} (mildly coupled to α_{p}), and, through the photomeson production opacity $\tau_{p\gamma}$, on the target photon energy density u'_t and the size R' of the emission region (see Fig. 2). The combination of these parameters is chosen to fit the observed neutrino flux (and hence is determined by observables), while each parameter individually is not required to be fixed. In case of target photon fields external to the jet particle-photon collisions may become anisotropic in the co-moving jet frame, which in turn affects the collision rates. The observed neu-

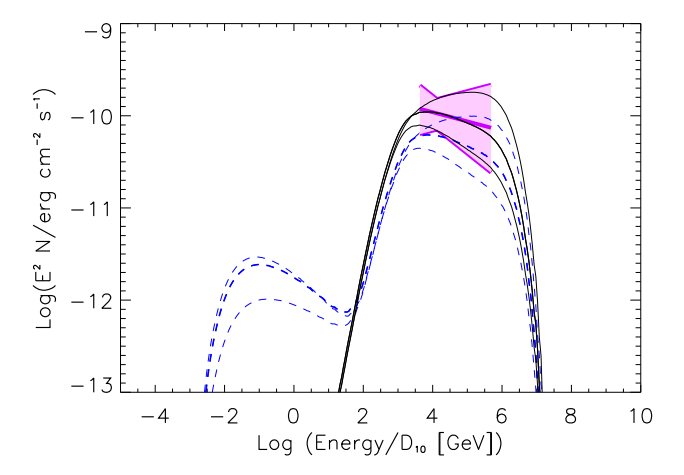


Figure 4. Effect of varying the proton distribution: Total neutrino (solid black line) and electron-positron yields (dashed blue line) at production due to proton-photon interactions (photo-meson and Bethe-Heitler pair production) on the same target photon field as for Fig. 3 for injection proton spectra with indices $\alpha_p = 1.8$, 2.0, and 2.1, with a normalization that is higher (lower) by $\sim 10\%$ for the harder (softer) spectrum and $E'_{\rm p,max} = 30$ PeV to reflect the spread of the total neutrino flux as measured by IceCube during the 2014 – 15 neutrino flare (violet bow tie), corrected for neutrino oscillations. Energies and fluxes are given in the observer frame.

trino flux level would then be matched by adjusting the injected proton energy density correspondingly.

Secondary pairs are produced along with the neutrinos, and are depicted as the blue dashed-line bump at high-energies (~ 0.1 TeV-10 PeV) in Fig. 3, while the produced gamma-ray spectrum from meson decay is shown by the solid blue line. The ratio of the secondary pair and photon number density to that of the neutrinos remains constant, even in the case of scatterings involving target photon populations that are anisotropic in the jet frame. Electromagnetic proton-photon interactions (Bethe-Heitler pair production) are guaranteed at sites where photo-hadronic interactions occur, and is therefore taken into account here (see Fig. 2).

We simulate Bethe-Heitler pair production in the same target photon field using the Monte Carlo code of Protheroe & Johnson (1996), and using the same proton injection distribution and flux normalization. The resulting pair yields upon production are shown as the blue dashed line lower-energy (10 MeV - 30 GeV) hump in Fig. 3 for a Doppler factor D=10 as an example, and its spread due to the observational uncertainties of the neutrino spectrum is depicted in Fig. 4. Note that the ratio of the pair-to-pion production rates in the same

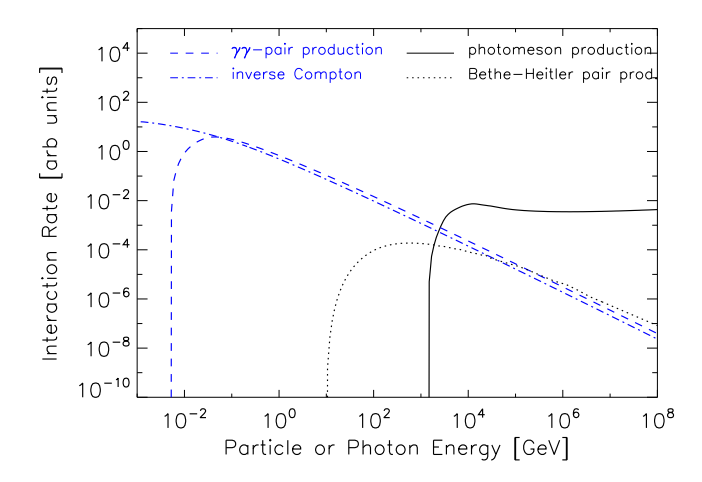


Figure 5. Mean particle-photon interaction rates in the same target photon field as used in Figs. 3 and 4. Photomeson production: solid black line, Bethe-Heitler pair production: dashed black line, inverse Compton scattering: dashed blue line, photon-photon pair production: dotted blue line. All energies are given in the jet frame.

target photon field (see Fig. 5) is fixed by the nature of the interaction.

Fig. 5 depicts interaction rates for various processes. It illustrates the dominance of losses due to Bethe-Heitler pair production for low proton energies while above the threshold for meson production photohadronic interactions dominate. While the minimal energy range of the target photon field is fixed to some extent by the energy range of the observed neutrino spectrum (modulo the Doppler factor in jetted neutrino sources) its shape is less constrained. Indeed, by choosing softer (e.g. $\alpha_t = 2 - 3$) or harder (e.g. $\alpha_t = 0 - 0.5$) power-law target photon fields we were able to find equally good representations of the observed neutrino spectrum, with only very small adjustments of the remaining parameters (e.g., α_p , etc). We attribute this behaviour to the narrowness of the observed neutrino spectrum. Changing the target photon spectral index in the considered narrow energy range is expected to cause only minor changes in the associated pair cascade spectrum (see Sect. 3.2), well within the uncertainties implied by the observed neutrino spectrum. The situation changes somewhat when extending sufficiently peaked target photon spectra to a broader energy range. For example, by extending the $\alpha_t = 1$ target photon spectrum down to $\epsilon'_{\min} = 1$ eV, we were also able to find a representation of the observed neutrino spectrum for $\alpha_p = 2.2$ and $E'_{p,\text{max}} = 20$ PeV. While the corresponding impact on the synchrotron-supported cascades turns out minor (except for a broadening of the absorption

troughs), the Compton-supported cascades will become broader (see Sect. 3.2.1).

Finally, varying the Doppler factor shifts the energy range of the minimal target photon field and injected proton spectrum correspondingly, while the required flux normalization to reach the observed neutrino flux level can be adjusted by changing the injected proton energy density accordingly. We scanned from D=1 (suitable for misaligned jetted AGN) up to D=50 (suggested by minute-time scale gamma-ray flux variations found in some blazars (e.g., Begelman et al. 2008) to find satisfactory representations of the observed neutrino spectrum by using $\epsilon'_{\rm min}=1\dots170~{\rm keV},\ \epsilon'_{\rm max}=4\dots1000~{\rm keV}$ and $E'_{\rm p,max}=3\dots300~{\rm PeV}.$

To summarize, Fig. 3 shows the distribution of all secondary pairs and γ -rays that are inevitably produced along with the (observed) neutrinos. By varying the proton spectral index $\alpha_p=2.0\pm^{0.1}_{0.2}$ we propagate the observed uncertainties of the neutrino spectrum to the corresponding pair and γ -ray distributions. These pairs and γ -rays typically initiate electromagnetic cascades (see Fig. 2) which re-distribute their power to energies where the produced photons can eventually escape the source. The $\gamma\gamma$ -pair production optical depth and its energy-dependence determines the spectral escape probability of the photons, and is therefore central for calculating the emerging photon spectrum associated with the neutrino spectrum.

3.2. Pair cascading

The high-energy pairs and γ -rays that were produced along with the neutrino flux in the minimal target radiation field are injected into a pair cascading code. In a radiative and magnetized environment the electromagnetic cascade develops rapidly in the target photon field through photon-photon pair production, and is either driven by mainly inverse Compton scattering in the same radiation field ('Compton-supported cascades') if $u'_{\rm t} \gg u'_{B}$ (with u'_{B} the magnetic field energy density), by synchrotron radiation ('synchrotron-supported cascades') if $u'_{\rm t} \ll u'_{\rm B}$, or by both ('synchrotron-Compton cascades') in cases where the magnetic field energy density turns out to be comparable to the target photon energy density (see Fig. 2). Once the cascade photons reach down to energies too low for pair production, the cascade development ceases, and the remaining pairs lose their energy via inverse Compton and/or synchrotron emission. The emerging photon spectrum is governed by both, the energy-dependent photon-photon pair production optical depth, and the dominating radiative dissipation process.

The pair cascading code employs the matrix multiplication method described by Protheroe & Stanev (1993) and Protheroe & Johnson (1996). Monte Carlo programs for photon-photon pair production and inverse Compton scattering are used to calculate the mean interaction rates (see Fig. 5) and the secondary particle and photon yields due to the interaction with the target radiation field. Note that inverse Compton scattering during the cascading proceeds in the Klein-Nishina regime, and transitions to the Thomson regime only below the threshold for pair production. The calculation of the synchrotron yields follows Protheroe (1990) (see also Pacholczyk 1970). The yields are then used to build-up transfer matrices which describe the change in the electron and photon spectra after propagating a given time step δt , which we chose as the dynamical time scale of the problem. The escape probability for photons is calculated using the formula given in Osterbrock & Ferland (2006) for a spherical region, while charged particles are assumed not to escape. For steady-state spectra we continue the transfer process until convergence is reached. In each time step energy conservation is verified.

In the following, all the photon models are generated with a normalization that yields the observed neutrino flux.

3.2.1. Compton-supported Cascades

If inverse Compton scattering supports the cascade $(u'_t \gg u'_B)$, the emerging photon spectra are fully determined once the opacity due to photon-photon pair production is fixed, because $\tau_{\gamma\gamma} \propto \tau_{\rm IC}$ (with $\tau_{\rm IC}$ the inverse Compton optical depth). This energy-dependent opacity in turn is related to the optical depth of photonproton interactions, which itself is linked to the neutrino spectral flux (see Sect. 3.1). Compton-supported cascading on the minimal target photon field (as determined in Sect. 3.1) therefore provides the corresponding minimal cascade flux for $u'_t \gg u'_B$. In the following we choose to vary the maximum of the energy-dependent photon-photon opacity, $\tau_{\gamma\gamma,\mathrm{max}}$ (which here serves as a proxy for $(R' \cdot u'_t)$ to calculate the corresponding cascade spectra. Figs. 6 – 9 show our results for Doppler factors $D = 1,10 \text{ and } 50 \text{ and } \log(\tau_{\gamma\gamma,\text{max}}) = -6, -5, \dots, 0, 1, 2,$ covering the optically thin and thick cases, and compares them to the MWL SED of TXS 0506+056 during the period of the neutrino flare. The shaded areas represent the spread of the cascade spectra (shown for selected $\tau_{\gamma\gamma,\text{max}} = 10^{-5}, 1, 100$ as examples) due to the uncertainties in the observed neutrino spectrum.

The cascade spectra at source (thin lines) are then corrected for absorption in the extragalactic background light (EBL) using the model of Franceschini & Rodighiero

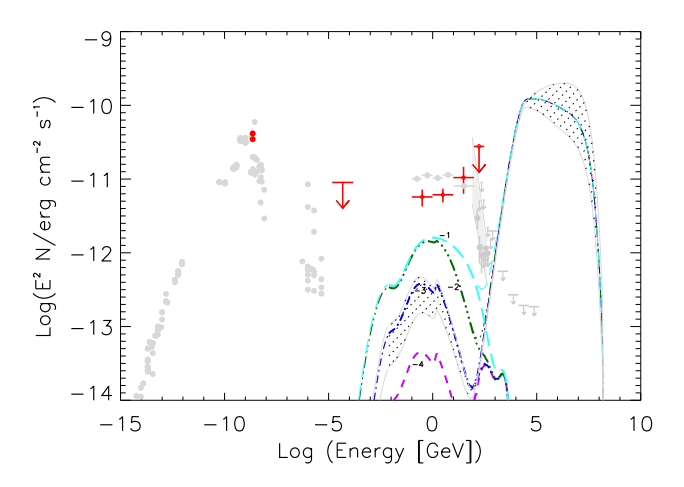


Figure 6. Compton-supported cascade spectra arriving at Earth without (thin lines) and including absorption in the EBL (thick lines) using the model of Franceschini & Rodighiero (2017) for $\log(\tau_{\gamma\gamma,\text{max}}) = -4$ (short dashed line), -3 (dashed-dotted line), -2 (dashedtriple-dotted line), -1 (long dashed line) as indicated, and D = 10. The shaded areas represent the spread of the cascade spectra, for the case $\tau_{\gamma\gamma,\text{max}} = 10^{-3}$ as an example, propagated from the uncertainties of the observed neutrino spectrum. The red data points (ASAS-SN, SWIFT-BAT, Fermi-LAT) depict the quasisimultaneous observations while the grey data points represent archival data (Aartsen et al. 2018a). VHE data (all MAGIC data from Ansoldi et al. (2018); all VERITAS data from Abeysekara et al. (2018), HAWC archival data from Aartsen et al. (2018a) are not simultaneous to the 2014/15 neutrino flare and are included in grey.

(2017). EBL-corrected cascade spectra are shown as thick lines. For $\tau_{\gamma\gamma,\text{max}} \ll 1$ (e.g., Fig. 6), internal absorption can be neglected, and the emerging inverse Compton flux increases with increasing opacity since $\tau_{\gamma\gamma} \propto \tau_{\rm IC}$. None of these cascade spectra reach the flux level of the MWL (in particular, Fermi-LAT) data. Therefore, in these cases, most of the photon flux has to be produced by emission processes occurring in the source that were not initiated by proton-photon interactions. When increasing the opacity further, $\tau_{\gamma\gamma} \gg 1$ (e.g., Fig. 7), deep absorption troughs in the GeV-range appear. Any photons in the GeV range produced cospatially to the neutrino flux, will inevitably suffer from internal absorption and will subsequently be cascaded to lower energies, independent of their production process. In this case of an efficient neutrino producer, the observed GeV-flux has to be produced either in a region within the jet of TXS 0506+056 that has no dense radiation fields at keV energies, or in a different source altogether. As a consequence, there is no causal connection between the observed neutrino flux and observed

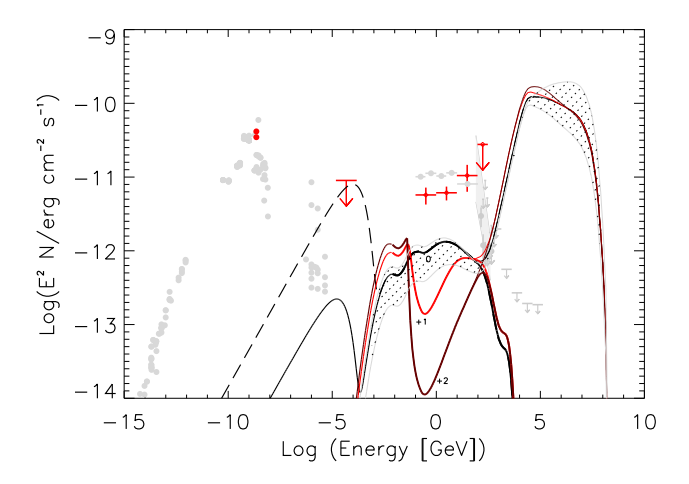


Figure 7. Compton-supported cascade spectra arriving at Earth without (thin lines) and including absorption in the EBL (thick lines) for $\log(\tau_{\gamma\gamma,\text{max}})=0,1,2$ as indicated, and D=10. The shaded areas represent the spread of the cascade spectra, for the case $\tau_{\gamma\gamma,\text{max}}=1$ as an example, propagated from the uncertainties of the observed neutrino spectrum. For the $\tau_{\gamma\gamma,\text{max}}=1$ -case we have also added the corresponding proton synchrotron radiation component for two sub-equipartion ($u_B' \ll u_t'$) field strengths: 0.5 G (solid line), 3 G (dashed line). The data points are the same as shown in Fig. 6.

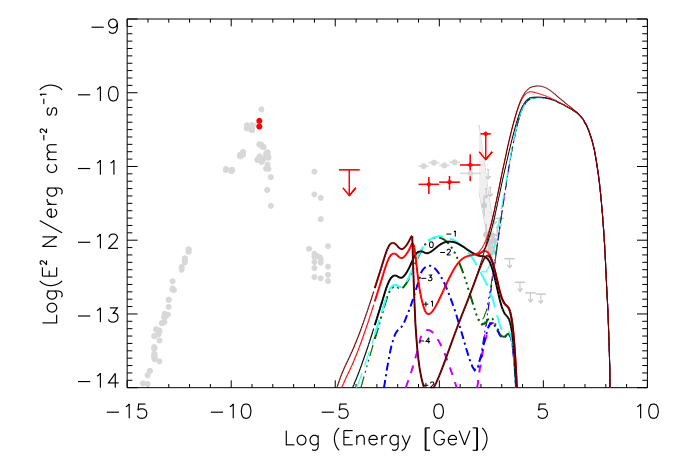


Figure 8. Compton-supported cascade spectra arriving at Earth without (thin lines) and including absorption in the EBL (thick lines) for $\tau_{\gamma\gamma,\text{max}} = 10^{-4}$ (short dashed line), 10^{-3} (dashed-dotted line), 10^{-2} (dashed-triple-dotted line), 10^{-1} (long dashed line), 1, 10, 100 (solid lines) as indicated, and D = 1. The data points are the same as shown in Fig. 6.

GeV-flux. These findings are similar for all values of the Doppler factor inspected (see Figs. 8-9).

As pointed out in Sect. 3.1 broader target radiation fields may also lead to photo-hadronically produced neu-

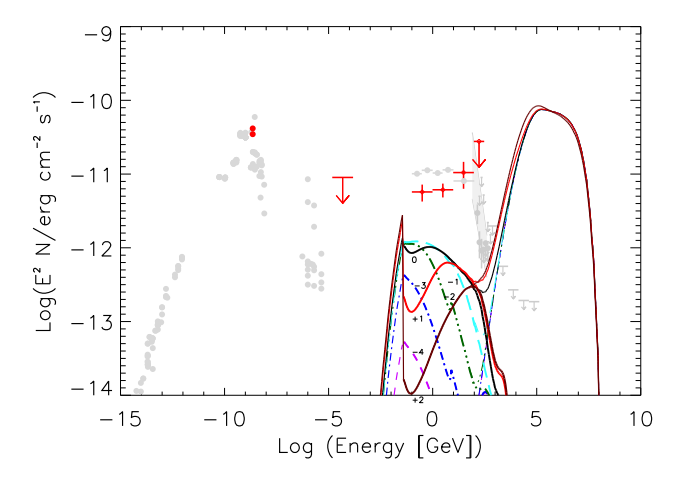


Figure 9. Compton-supported cascade spectra arriving at Earth without (thin lines) and including absorption in the EBL (thick lines) for $\tau_{\gamma\gamma,\text{max}} = -4$ (short dashed line), -3 (dashed-dotted line), -2 (dashed-triple-dotted line), -1 (long dashed line), 0, 1, 2 (solid lines) as indicated, and D=50. The data points are the same as shown in Fig. 6.

trino spectra that fit the observations (e.g., extending the target field $n_t' \propto \epsilon'^{-1}$ to lower energies, e.g., $\epsilon'_{\min} = 1 \, \mathrm{eV}$). Inspecting the associated Compton-supported cascade spectra shows broader SEDs than for the case of narrow target photon fields (see Fig. 10). This is because the photon energy associated with the lowest-energy radiating electron is lower for $\epsilon'_{\min} = 1 \, \mathrm{eV}$ (broad target field) than for $\epsilon'_{\min} = 10 \, \mathrm{keV}$ (narrow target field). In addition, the overall cascade flux increases notably below the GeV regime when increasing the energy range of the target photon field. We note that in such cases X-ray data may be able to place stringent constraints on models.

The Compton optical depth $\tau_{\rm IC}$ may be altered when scatterings sample photon fields that are anisotropic in the co-moving frame. Since $\tau_{\rm IC}$ is directly linked to $\tau_{\gamma\gamma}$ (see Fig. 5) and the emerging cascade spectra presented here are proxied by $\tau_{\gamma\gamma}$, no significant changes of the Compton cascade spectra for a given $\tau_{\gamma\gamma}$ are expected in such cases.

3.2.2. Synchrotron-supported Cascades

If the magnetic energy density u_B' is much larger than the target photon field energy density u_t' the electromagnetic cascades are supported by synchrotron radiation. In blazar jet environments the magnetic field strength B (assumed constant here) is typically $\ll B_{\rm cr} = 2\pi m_e^2 c^3/(eh) = 4.4 \times 10^{13}$ G, the critical magnetic field strength for radiating pairs, which is therefore also our assumption here. As an example we show in Figs. 11 – 13 the case where $u_B' = 10\,u_t'$ with the above spec-

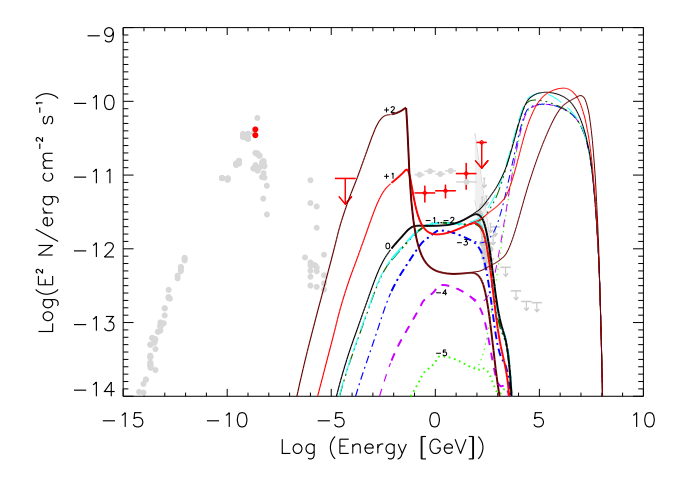


Figure 10. Spectra from Compton-supported cascading in a broader target photon field ($\epsilon'_{\min} = 1 \text{eV}$, $\epsilon'_{\max} = 60 \text{keV}$, $\alpha_t = 1$) arriving at Earth without (thin lines) and including absorption in the EBL (thick lines) for $\log(\tau_{\gamma\gamma,\max}) = -5$ (dotted line), -4 (short dashed line), -3 (dashed-dotted line), -2 (dashed-triple-dotted line), -1 (long dashed line), 0, 1, 2 (solid lines) as indicated, and D = 10. The data points are the same as shown in Fig. 6.

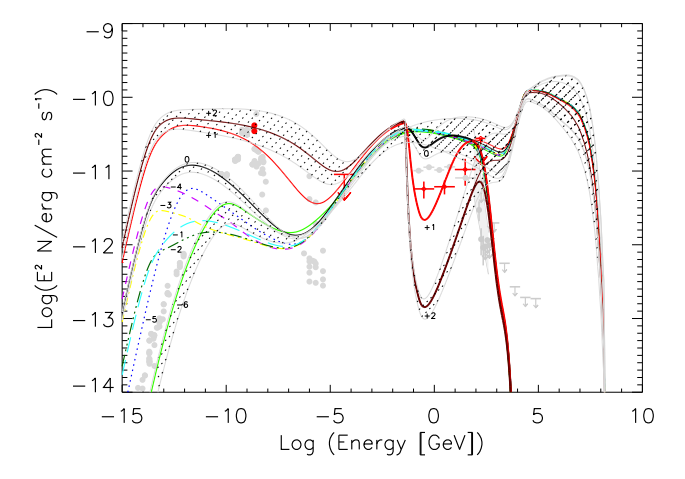


Figure 11. Synchrotron-supported cascade spectra arriving at Earth without (thin lines) and including absorption in the EBL (thick lines) for $u_B = 10u'_{\rm target}$ and $\log(\tau_{\gamma\gamma,\rm max}) = -6$ (solid line), -5 (dotted line), -4 (short dashed line), -3 (dashed-dotted line), -2 (dashed-triple-dotted line), -1 (long dashed line), 0, 1, 2 (solid lines) as indicated, and D=10. The shaded areas represent the spread of the cascade spectra, for the cases $\tau_{\gamma\gamma,\rm max}=10^{-6},1,100$ as examples, propagated from the uncertainties of the observed neutrino spectrum. The data points are the same as shown in Fig. 6.

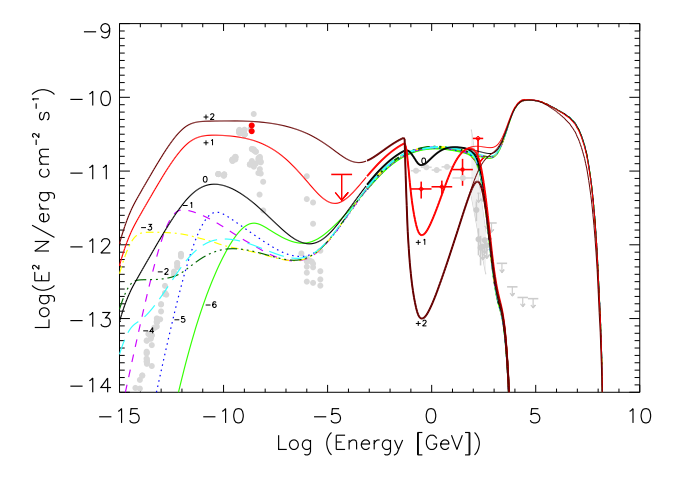


Figure 12. Same as Fig. 11 except D = 1.

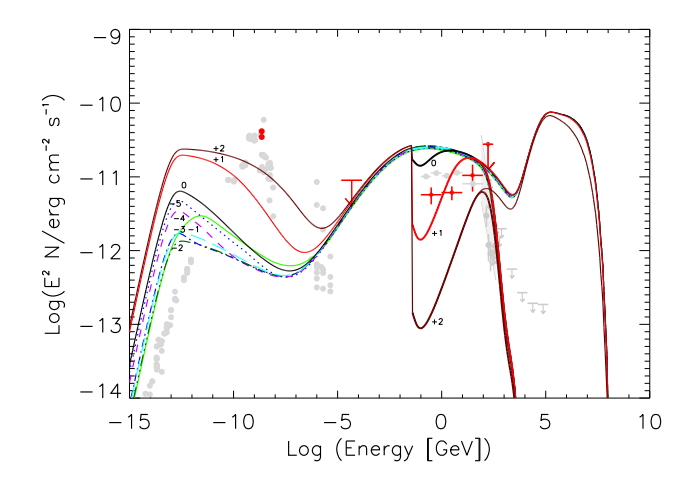


Figure 13. Same as Fig. 11 except D = 50.

ified target photon spectrum, again corrected for absorption in the EBL. Synchrotron-self absorption is not taken into account. The uncertainties in the IceCubeflux are propagated again to the corresponding cascade spectra, and depicted in Figs. 11 - 13 as shaded areas for the cases $\tau_{\gamma\gamma,\text{max}} = 10^{-6}, 1, 100$. In the optically thin case the standard synchrotron cooled spectra for a two-component (meson-decay and the lower energy Bethe-Heitler pairs) pair population is recovered, with increasing cooling for increasing field strength (see Fig. 14). Note that for $B \ll B_{\rm cr}$ the energy loss rate is $\propto \gamma_e^2$ for all energies whereas for Compton-loss dominated pair cascades the interaction probability changes from $\propto \gamma_e$ in the Klein-Nishina regime to $\propto \gamma_e^2$ in the Thomson regime. This is reflected in the resulting shape of the cascade spectra. Because the secondary pair distribution resulting from proton-photon interactions is

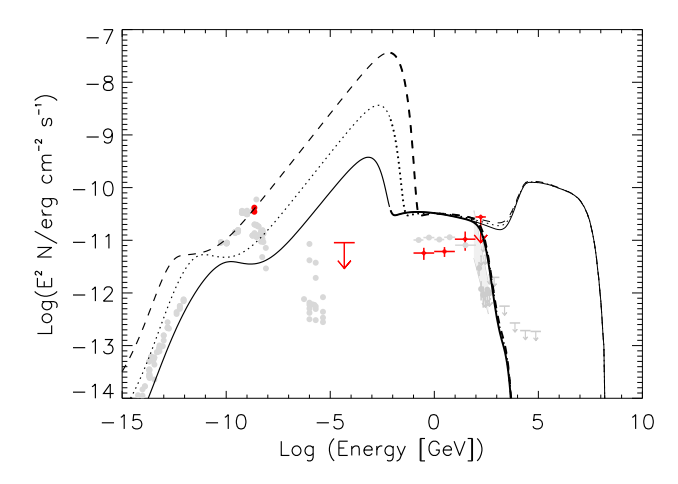


Figure 14. Synchrotron-supported cascade spectra, including the proton synchrotron radiation components, arriving at Earth without (thin lines) and including absorption in the EBL (thick lines) for $u'_B = 10u'_t$ (solid line), $u'_B = 10^2u'_t$ (dotted line), $u'_B = 10^3u'_t$ (dashed line), $\tau_{\gamma\gamma,\text{max}} = 10^{-6}$, and D = 10. The data points are the same as shown in Fig. 6.

fixed by the observed neutrino spectrum the corresponding synchrotron-supported cascade emission in the optically thin case is expected to be unaffected by a possible anisotropy of the collisions. In the optically thick case, $\tau_{\gamma\gamma} \gg 1$, the number of pairs, produced from synchrotron photons, increases dramatically in the cascade. The amount of reprocessing is given by $\tau_{\gamma\gamma}$, and the resulting cascade flux for a given $\tau_{\gamma\gamma}$ is therefore independent of whether it is produced by isotropic or anisotropic scatterings, as long as the contribution to the scattering rate per unit scattering angle is energyindependent. Also, the produced pairs are more energetic in environments with high magnetic fields than in sites of low magnetization (see Fig. 15). Similarly as for the optically thick Compton-supported cascades we note deep absorption troughs at GeV energies leading to the same implications for the association between the neutrino and GeV-source, i.e., the lack of a causal connection between the observed neutrino and GeV-flux. Note that the hump-like feature at high energies ($\sim 1 \text{GeV}$ -1TeV) in the optically thick cases disappears by sufficiently broadening the target photon spectrum to lower As compared to the Compton-supported energies. case, the synchrotron-supported cascades extend down to much lower energies: whereas the inverse Compton photon spectrum extends down to $\propto \gamma_{min}^2 \epsilon'_{t,min}$, for the synchrotron spectrum the lowest energy reached is \propto $\gamma_{min}^2(B/B_{\rm cr})m_ec^2$ with typically $(B/B_{\rm cr})m_ec^2\ll\epsilon_{t,\rm min}'$ for an observed neutrino spectrum extending down to tens of TeV.

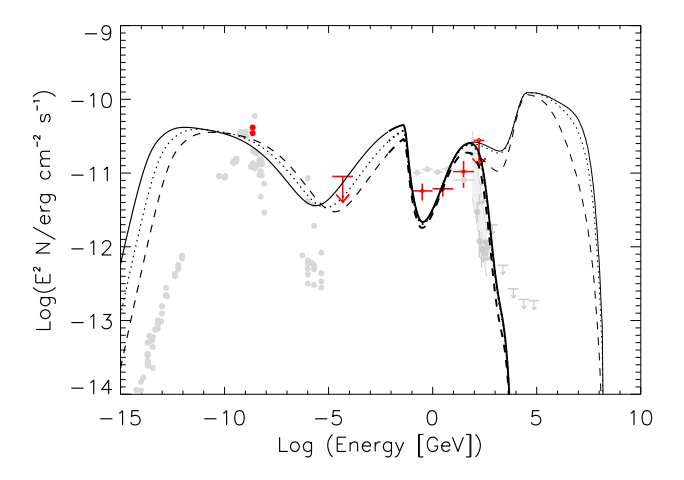


Figure 15. Synchrotron-supported cascade spectra arriving at Earth without (thin lines) and including absorption in the EBL (thick lines) for $u_B' = 10u_t'$ (solid line), $u_B' = 10^2u_t'$ (dotted line), $u_B' = 10^3u_t'$ (dashed line), $\tau_{\gamma\gamma,\text{max}} = 10$, and D = 10. The data points are the same as shown in Fig. 6.

When compared to the quasi-simultaneous observed SED we note that deep optical-to-X-ray observations are able to provide sensitive constraints, in particular on the efficiency of neutrino production. For the present case we find that the BAT upper limit constrains the neutrino-producing environment to $\tau_{\gamma\gamma, \rm max} < 100$ for $D \leq 10$, whereas the Fermi-LAT spectrum excludes $\tau_{\gamma\gamma, \rm max} < 10$.

3.2.3. Synchrotron-Compton Cascades

Generally in environments where $u_B' \sim u_{\mathrm{t}}'$ both, synchrotron as well as Compton losses have to be considered when following electromagnetic cascades. In the high-energy regime, down to the threshold for pair production, the synchrotron-Compton (see Figs. 16 – 18) and synchrotron-supported cascade SEDs are very similar. This is because Compton-scattering proceeds in the Klein-Nishina regime here at a rate much smaller than the synchrotron loss rate, and the resulting spectra are determined by synchrotron radiation and pair production. At lower energies, photon production takes place through synchrotron and inverse Compton scattering on equal footing, which is reflected in the resulting cascade spectra. With increasing opacity the number of (cascade) pairs rises. At MeV-energies the resulting SED is dominated by inverse Compton photons from the primary Bethe-Heitler pairs and cascade pairs, and synchrotron photons from the π^{\pm} -decay pairs, while the SED at lower einergies is due to synchrotron radiation from the Bethe-Heitler and cascade pairs.

By comparing also here with the quasi-simultaneous observed SED we find again the BAT upper limit to

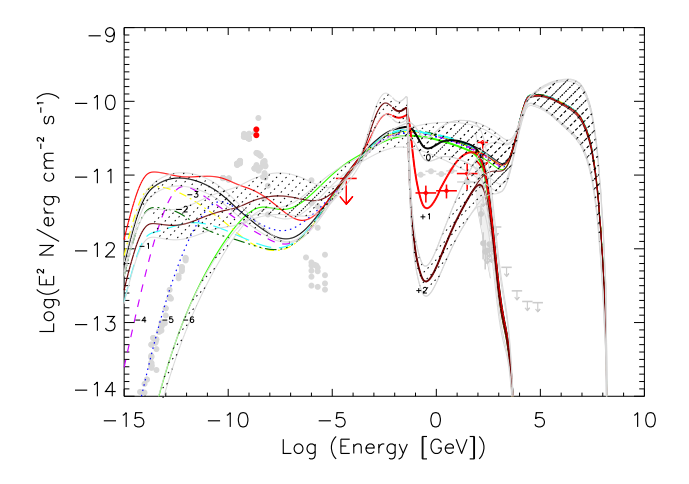


Figure 16. Synchrotron-Compton cascade spectra arriving at Earth without (thin lines) and including absorption in the EBL (thick lines) for $u_B = u'_{\rm target}$ and $\tau_{\gamma\gamma,{\rm max}} = 10^{-6}$ (solid line), 10^{-5} (dotted line), 10^{-4} (short dashed line), 10^{-3} (dashed-dotted line), 10^{-2} (dashed-triple-dotted line), 10^{-1} (long dashed line), 1, 10, 100 (solid lines) as indicated, and D=10. The shaded areas represent the spread of the cascade spectra, for the cases $\tau_{\gamma\gamma,{\rm max}}=10^{-6},1,100$ as examples, propagated from the uncertainties of the observed neutrino spectrum. The data points are the same as shown in Fig. 6.

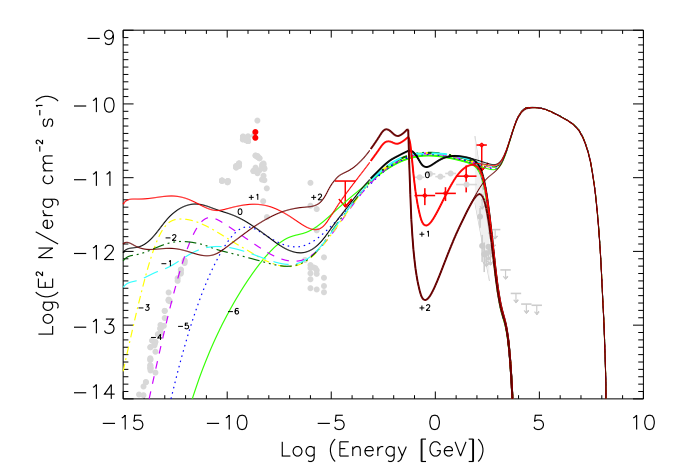


Figure 17. Same as Fig. 16 except D = 1.

place constraints on the neutrino production efficiency $\tau_{p\gamma}$: Only $\tau_{\gamma\gamma,\mathrm{max}}\sim$ a few tens for small Doppler factors $D<10,~\tau_{\gamma\gamma,\mathrm{max}}\sim10$ if $D=10,~\mathrm{and}~\tau_{\gamma\gamma,\mathrm{max}}\sim$ a few hundreds for large $D\gg10$ do not violate the minimal cascade fluxes computed, similar as for the synchrotron-supported cascades.

3.3. On efficient neutrino production

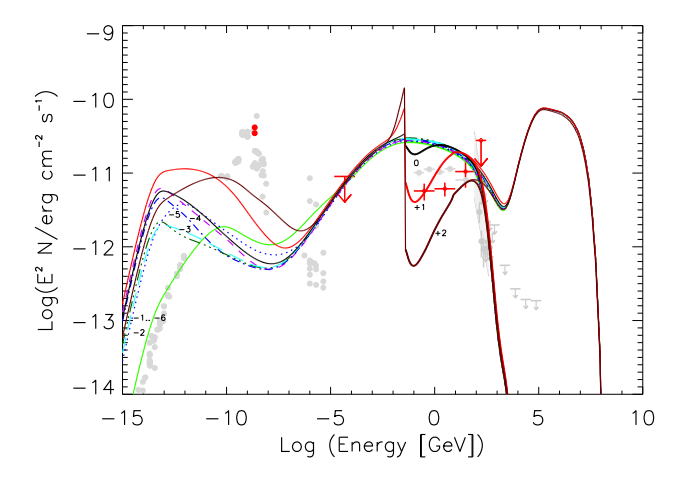


Figure 18. Same as Fig. 16 except D = 50.

Since the cross section maximum for photon-photon pair production (near its threshold) compares to the maximum cross section value for photomeson production (at the Δ_{1232} -resonance near threshold) as $\sigma_{\gamma\gamma,\text{max}} \approx 300\,\sigma_{p\gamma,\text{max}}$, we expect in typical AGN environments the maximum optical depth of the respective interactions in the same target photon field to approximately scale correspondingly. In particular, for the case of an efficient neutrino producer, i.e., $\tau_{p\gamma} > 1$, one yields $\tau_{\gamma\gamma} \gg 1$, and deep absorption troughs appear in the SED at energies E'_{γ} where $\gamma\gamma$ -pair production sets in (see also discussions in, e.g., Begelman et al. (1990); Dermer et al. (2007); Murase et al. (2016)):

$$E'_{\gamma,\text{thr}} = \frac{s_{\gamma\gamma,\text{thr}}}{2\epsilon'(1-\cos\theta)} = \frac{4m_e^2c^4}{2\epsilon'(1-\cos\theta)}$$
(1)

where $\sqrt{s_{\gamma\gamma,\rm thr}}$ is the center-of-momentum-frame threshold energy of the interaction, ϵ' the target photon energy and θ the interaction angle. Considering that neutrinos are produced in the same target photon field via photomeson production dominantly in the Δ -resonance region, the energy of the target photons is related to the observed neutrino energy $E_{\nu,\rm obs}$ through

$$\epsilon' \gtrsim \frac{s_{\Delta} - m_p^2 c^4}{2E_p' (1 - \cos \theta)} = \frac{(s_{\Delta} - m_p^2 c^4) \xi D}{2E_{\nu, \text{obs}} (1 - \cos \theta)}$$
 (2)

with $s_{\Delta} \simeq (1.232 \, {\rm GeV})^2$ and assuming $\beta_p = 1$. Note that the interaction angle for proton-photon and photon-photon interactions is in this case expected to be similar for highly relativistic protons. By combining equations (1) and (2) one can then relate the (observer frame) photon energy $E_{\gamma, {\rm obs}}$ to the detected neutrino energy through

$$E_{\gamma,\text{obs}} \lesssim \frac{4m_e^2 c^4 E_{\nu,\text{obs}}}{(s_\Delta - m_p^2 c^4)\xi} \approx 3.3 \cdot 10^{-5} E_{\nu,\text{obs}} \xi_{0.05}^{-1} \,.$$
 (3)

If neutrinos are very efficiently produced photohadronically, the associated cascade photons therefore can only escape the source at energies $\lesssim E_{\gamma,\rm obs}$. For a neutrino flare spectrum in the 30 TeV – 3 PeV range, the corresponding cascade spectrum is hence expected at \ll 1 GeV. This applies also to > GeV photons from alternative radiation processes. As a consequence, one does not expect a causal connection between the GeV-flux detected by the LAT from TXS 0506+056 and the observed 'flare' IceCube neutrinos for an efficient neutrino producer, irrespective of the dominant dissipation process.

4. IMPLICATIONS ON THE JET POWER AND TARGET PHOTON FIELDS

We now derive constraints on the jet power using the observed neutrino flux in combination with limits for their production efficiency, derived via the minimal cascading flux (see Sect. 3.2). This can then be used, in a subsequent step, to deduce limits on the origin of the target photon field. Here, we will distinguish two possible scenarios, which can be thought of as extreme, limiting cases: (a) a target photon field that is comoving with the emission region (such as the electronsynchrotron emission), or (b) a stationary target photon field in the AGN rest frame. In case (a), the target photon energy ϵ'_t corresponds to an observed photon energy of $\epsilon_{\text{obs}} \geq 16D_1^2 \xi_{0.05}/E_{14} \text{ keV (i.e., hard X-rays)},$ while in case (b), the external (stationary) target photon field is Doppler boosted into the blob frame, so that $\epsilon_{\rm obs} \geq 0.16 \xi_{0.05} / E_{14} \text{ keV (i.e., UV-to-soft X-rays)}.$

4.1. Target Photon Energy Density and Proton Kinetic Power

As in Section 3 we consider a proton spectrum of the form $N_p(\gamma_p) = N_0 \gamma_p^{-\alpha_p}$ with $\alpha_p = 2$. The co-moving neutrino luminosity (see Sect. 2.1) can be related to the proton energy loss rate due to photopion production, given by Kelner & Aharonian (2008)

$$\dot{\gamma}_{p,p\gamma} \approx -c \left\langle \sigma_{p\gamma} f \right\rangle n'_{ph}(\epsilon'_t) \, \epsilon'_t \, \gamma_p \tag{4}$$

where $\epsilon'_t = \epsilon'/(m_e c^2)$ and $\langle \sigma_{p\gamma} f \rangle \approx 10^{-28} \text{ cm}^2$ is the inelasticity-weighted p γ interaction cross section. The factor $n'_{\rm ph}(\epsilon'_t)\,\epsilon'_t$ provides a proxy for the co-moving energy density of the target photon field, $u'_{\rm t} \approx m_e c^2 \, n'_{\rm ph}(\epsilon'_t)\,\epsilon'_t$. Considering that the energy lost by protons in p γ interactions is shared approximately equally between photons and neutrinos, the 30 TeV – 3 PeV neutrino luminosity is given by

$$L_{
u}' pprox rac{1}{2} N_0 \, m_p c^2 \int\limits_{\gamma_1}^{\gamma_2} \gamma_p^{-lpha_p} \, \left| \dot{\gamma}_{
m p,p\gamma}
ight| \, d\gamma_p$$

$$\approx 1.3 \times 10^{-14} N_0 u_t' \,\mathrm{cm}^3 \,\mathrm{s}^{-1}$$
 (5)

for $\alpha_p=2$. The limits in the integral in Eq. (5) are given by $\gamma_1=6.4\times 10^4(D_1\xi_{0.05})^{-1}$ and $\gamma_2=6.4\times 10^6(D_1\xi_{0.05})^{-1}$, and $\alpha_p=2$. Setting the neutrino luminosity from Eq. (5) equal to the co-moving neutrino luminosity inferred from IceCube observations, yields

$$N_0 u_t' \approx 1.3 \times 10^{57} D_1^{-4} \,\mathrm{erg} \,\mathrm{cm}^{-3}$$
 (6)

We now have two independent constraints on the target photon field: First is the direct observational constraint that the observed photon flux corresponding to the target photon field can not exceed the observed flux in the relevant energy range. This provides a direct upper limit on u'_t , and will be used in Sect. 4.2, 4.3.

Second is the limit on the $\gamma\gamma$ opacity provided by the target photon field. In Sect. 3.2, we had found that, in order not to violate constraints from the observed optical, X-ray and/or Fermi-LAT flux, the system needs to be either in a regime where cascades are Compton dominated (as the minimal level of the Compton cascade emission turned out to lie always below the observed SED, irrespective of the value of $\tau_{\gamma\gamma, \rm max}$, or synchrotron (or Compton-synchrotron) dominated for $\tau_{\gamma\gamma, \rm max} \sim$ a few 10 (100) for small $D \leq$ 10 (large $D \gg$ 10) Doppler factor. Compton-supported cascades will occur if

$$u_t^{'\text{Comp}} \gg u_B' \approx 4 B_1^2 \text{ erg cm}^{-3}.$$
 (7)

in the co-moving frame with $B=B_110\mathrm{G}$ the magnetic field strength.

Using a simple δ -function approximation for the $\gamma\gamma$ pair production cross section, we can estimate $\tau_{\gamma\gamma,\text{max}} \sim \sigma_T u_t' R'/(3 m_e c^2) \sim 2.7 \times 10^{-3} u_0 R_{16}$, where $u_0 = u_t'/(\text{erg cm}^{-3})$ parameterizes the target photon energy density, and $R_{16} = R'/(10^{16} \text{ cm})$ is the size of the emission region. Thus, the condition $\tau_{\gamma\gamma,max} \sim$ a few 10 (100) for $D \leq 10$ ($D \gg 10$) translates into a limit of

$$u_t^{\prime \text{Syn}} \lesssim 10^4 R_{16}^{-1} \text{ erg cm}^{-3} \text{ for } D \leq 10,$$

 $u_t^{\prime \text{Syn}} \lesssim 10^5 R_{16}^{-1} \text{ erg cm}^{-3} \text{ for } D \gg 10.$ (8)

Combining with $u_t' \leq u_B' \approx 4 B_1^2 \text{ erg cm}^{-3}$ for Synchrotron-(Compton-synchrotron) cascades one gets:

$$R_{16}B_1^2 > 2.5 \cdot 10^3 (2.5 \cdot 10^4)$$
 for $D < 10(D \gg 10)$ (9)

This indicates the need for large field strengths and/or emission regions in the case of Synchrotron-(Compton-synchrotron) cascades operating in the source.

A limit on the proton kinetic power can then be derived by combining Eq. 6 with Eq. 8 in case Synchrotron-(Compton-synchrotron) cascades determine the dissipation process. The co-moving relativistic proton energy

density, assuming that the proton spectrum extends as an unbroken power-law with index $\alpha_p = 2$ from $\gamma_{\min} = 1$ to $\gamma_2 \gg \gamma_{\min}$, is calculated by

$$u'_{p} = m_{p}c^{2}V'^{-1}N_{0}\int_{1}^{\gamma_{2}}d\gamma_{p}\gamma_{p}^{1-\alpha_{p}}$$

$$\approx 3.6 \times 10^{-52} N_0 R_{16}^{-3} (15.7 - \eta) \,\mathrm{erg} \,\mathrm{cm}^{-3}$$
 (10)

with $\eta = \ln(D_1\xi_{0.05})$, and V' the co-moving volume of the emission region. Since typically $\eta \approx 0$ with only small deviations expected, we will neglect the η -term in the following. The relativistic proton kinetic power $L_p = 2\pi R'^2 c \Gamma^2 u_p'$ carried by the jet in highly magnetized environments where pair synchrotron losses can not be neglected can then be evaluated as

$$L_p \gg 1.4(14) \cdot 10^{47} (\Gamma_1/D_1^2)^2 \,\mathrm{erg \, s^{-1}} \text{ for } D \gg 10 (D \le 10),$$
(11)

with Γ the bulk Lorentz factor $\Gamma \equiv 10 \Gamma_1$, and a magnetic field power (using Eq.9) of

$$L_B \gg 0.2(2) \cdot 10^{50} \Gamma_1^2 R_{16} \,\mathrm{erg \, s^{-1}} \,\mathrm{for} \,D \le 10(D \gg 10).$$
 (12)

Hence, the total jet power turns out to be in this case at least of order $\sim 10^{49...50} {\rm erg \, s^{-1}}$ (or higher), independent of the origin of the target photon field.

We now use the observed SED in the energy range of the target photons (here $\epsilon'_{\min} = 1...170$ keV, $\epsilon'_{\max} = 4...1000$ keV for D=1...50) to derive a direct limit on u'_t which will then be combined with the previous constraints.

4.2. Case a: Co-Moving Target Photon Field

If the target photon field is co-moving with the emission region, the required target photon energy corresponds to hard X-rays at an observed energy of $\epsilon_{\rm obs} \geq 16D_1^2\xi_{0.05}/E_{14}$ keV. The observed X-ray flux from TXS 0506+056 is of the order of $F_X^{\rm obs} \sim 10^{-12}$ erg cm⁻² s⁻¹, implied from archival data. The flux received directly from the target photon field, present in an assumed spherical emission region of size $R_t' \equiv 10^{16}\,R_{t,16}$ cm is $F_a^{\rm obs} = \frac{R_t'^2}{d_L^2}\,c\,u_t'\,D^4$ and must be equal to or less than the observed value. This constrains the co-moving target photon energy density to be

$$u_t' \lesssim 9 \times 10^{-4} R_{t,16}^{-2} D_1^{-4} \,\mathrm{erg} \,\mathrm{cm}^{-3}$$
 (13)

and in turn the proton-spectrum normalization factor in Eq. 6:

$$N_0 \gtrsim 1.5 \times 10^{60} R_{t.16}^2$$
 (14)

The corresponding total kinetic power carried by the jet can then be evaluated as

$$L_{\nu} \gtrsim 1.55 \times 10^{55} \,\Gamma_1^2 \, R_{t.16} \,\mathrm{erg \, s^{-1}}.$$
 (15)

which appears unreasonably high to be powered by an AGN accretion flow, as it exceeds the Eddington luminosity of even the most massive known supermassive black holes $(M_{\rm bh} \lesssim 10^{10}\,M_{\odot})$ by several orders of magnitude.

The photon energy density limit from Eq. (13) can also be used to calculate the proton cooling time scale due to photopion production:

$$t_{p\gamma}^{\text{obs}} = \frac{m_e c^2}{D c \langle \sigma_{p\gamma} f \rangle u_t'} \gtrsim 3 \times 10^{13} R_{t,16}^2 D_1^3 \text{ s}$$
$$\sim 9.5 \times 10^5 R_{t,16}^2 D_1^3 \text{ yr}$$
(16)

to compare with proton synchrotron cooling. The importance of proton synchrotron radiation in the context of hadronic AGN models has been first noticed by Mücke & Protheroe (2000); Aharonian (2000); Mücke & Protheroe (2001). Eq. 16 indicates that photopion production is several orders of magnitude less efficient than proton synchrotron radiation with a cooling time scale of

$$t_{psyn}^{\text{obs}} \simeq 9 \times 10^8 \, B_1^{-2} \, D_1^{-1} \left(\frac{\gamma}{6 \times 10^6} \right) \, \text{s} \,,$$
 (17)

even for protons of moderate Lorentz factors of $\gamma_p \sim 6 \times 10^6$. In fact, this allows us to calculate the relative radiative power output in proton synchrotron versus photo-pion induced emissions:

$$\frac{L_{\text{psy}}}{L_{p\gamma}} \sim \frac{t'_{p\gamma}}{t'_{psy}} \sim 4 \times 10^4 \, R_{t,16}^2 \, D_1^4 \, B_1^2 \left(\frac{\gamma}{6 \times 10^6}\right) \quad (18)$$

with proton synchrotron emission peaking at

$$\nu_{\rm psy}^{\rm obs} \sim 9 \times 10^{16} \, B_1 \, \left(\frac{\gamma}{6 \times 10^6}\right)^2 \, D_1 \, {\rm Hz}$$
 (19)

i.e., in the EUV/soft X-ray band. This implies that, in this scenario, the protons producing the 0.03-3 PeV neutrino flux are expected to produce proton synchrotron emission in the X-ray regime at a νF_{ν} flux value larger than the corresponding νF_{ν} neutrino flux value by a factor given by Eq. (18). Reducing this to the limit based on the observed X-ray flux $(L_{\rm psy}/L_{p\gamma} \lesssim 0.1)$ would require an unusually low magnetic field value $(B \lesssim 1~{\rm G})$ and/or a very low Doppler factor $D \sim 1$. This is demonstrated in Figs. 6, 13 where we have added the proton synchrotron radiation on top of the minimal cascade component for various model parameters.

Based on these results, we may confidently rule out a scenario in which the IceCube neutrino flare flux from TXS 0506+056 is photo-hadronically produced in a target photon field that is co-moving with the emission (and neutrino production) region.

4.3. Case b: Stationary Target Photon Field in the AGN Frame

In the case of a target photon field that is stationary in the AGN rest frame, the target photon energy (in the AGN frame) should be $\epsilon_{\rm obs} \geq 0.16 D_1 \xi_{0.05}/E_{14}$ keV, and the AGN-frame radiation energy density is boosted into the co-moving frame as $u_t' \approx \Gamma^2 u_t$. In the external-photon-field case, the spatial extent of the photon field may be scaled in units of a typical BLR size, $R_t \equiv 10^{17} R_{t,17}$ cm (AGN frame), and the corresponding flux received is $F_{UV}^{\rm obs} = \frac{R_t^2}{d_t^2} c \, u_t' \, \Gamma^{-2}$.

For the Compton-dominated cascade case we now insert the energy density from Eq. 7 to derive

$$F_{UV}^{\text{obs}} \gg 4.3 \cdot 10^{-13} (B_1 R_{t,17} / \Gamma_1)^2 \text{erg cm}^{-2} \text{ s}^{-1}$$
 (20)

which is below the observed SED from archival data for not too large field strengths. Inspecting now the case for a highly magnetized environment where synchrotron losses become non-negligible we derive a UV – soft X-ray flux of

$$F_{UV}^{\text{obs}} \gg (10^{-9} \dots 10^{-8}) R_{16}^{-1} (R_{t,17}/\Gamma_1)^2 \text{erg cm}^{-2} \text{s}^{-1}$$
(21)

for $D \leq 10$ ($D \gg 10$) by making use of Eq. 8. This flux level seems several orders of magnitude higher than the observed SED from archival data implies, and hence gives strong arguments to rule out an environment of the neutrino emission region where Synchrotron-(Comptonsynchrotron) cascades operate.

From the observed SED a conservative upper limit on the νF_{ν} flux at UV – soft X-rays may be placed at $\nu F_{\nu} \lesssim 10^{-11} \ {\rm erg \ cm^{-2} \ s^{-1}}$. The co-moving target photon energy density can then be constrained as

$$u_t' \lesssim 94 \,\Gamma_1^2 \, R_{t,17}^{-2} \, \text{erg cm}^{-3}$$
 (22)

giving a corresponding pair production optical depth of

$$\tau_{\gamma\gamma,\text{max}} \lesssim 0.25 \, R_{16} \, \Gamma_1^2 \, R_{t,17}^{-2}$$
(23)

and a photohadronic optical depth of

$$\tau_{p\gamma,\text{max}} \lesssim 8 \cdot 10^{-4} R_{16} \Gamma_1^2 R_{t,17}^{-2}$$
(24)

above the thresholds of the interactions. For moderate magnetic fields, $B \lesssim 10$ G, this may lead to Compton-supported cascades, thus not violating limits on the multi-wavelength cascade flux. Eq. (6) then constrains the proton-spectrum normalization to

$$N_0 \gtrsim 1.4 \times 10^{55} D_1^{-4} \Gamma_1^{-2} R_{t,17}^2$$
 (25)

yielding a required proton kinetic jet power of

$$L_p \gtrsim 1.5 \times 10^{50} \, D_1^{-4} \, R_{t,17}^2 \, R_{16}^{-1} \, \text{erg s}^{-1}.$$
 (26)

Due to the strong inverse dependence on the Doppler factor, for D significantly exceeding 10 (and/or a larger target-photon-field radius or smaller emission-region size), this may be within the range plausibly powered by accretion onto a supermassive black hole of mass $\sim 3 \cdot 10^8 \rm M_{\odot}$ (Padovani et al. 2019). The relativistic proton power from Eq. (26) may be compared to the power carried along the jet in magnetic fields,

$$L_B = 3.8 \times 10^{45} R_{16}^2 \Gamma_1^2 B_1^2 \,\mathrm{erg \, s^{-1}}.$$
 (27)

Thus, for $B \lesssim 10$ G, the jet would have to be strongly dominated by kinetic power of the relativistic protons.

For the target photon field of Eq. (22), the proton photopion cooling time scale is, analogous to Eq. (16),

$$t_{p\gamma}^{\text{obs}} \gtrsim 2.9 \times 10^9 \,\Gamma_1^{-2} \,R_{17}^2 \,\text{s} \sim 92 \,\Gamma_1^{-2} \,R_{17}^2 \,\text{yr}.$$
 (28)

Also in this case, proton-synchrotron radiation, at X-ray frequencies according to Eq. (19), can not be neglected, and the ratio of proton-synchrotron to photopion induced radiative (and neutrino) output will be

$$\frac{L_{\text{psy}}}{L_{p\gamma}} \gtrsim 0.4 \, \Gamma_1^{-2} \, D_1 \, R_{t,17}^2 \, B_1^2 \, \left(\frac{\gamma}{6 \times 10^6}\right)$$
 (29)

thus predicting X-ray proton-synchrotron emission with a flux of $\nu F_{\nu}(X) \gtrsim 10^{-10} \, \Gamma_1^{-2} \, D_1 \, R_{t,17}^2 \, B_1^2 \, (\gamma/[6 \times 10^6])$ erg cm⁻² s⁻¹. For a magnetic field of $B \sim$ a few G, this does not seem to violate observational limits (see also Fig. 6).

We thus conclude that a scenario in which an external soft X-ray photon field provides the targets for photo-pion reactions producing the IceCube neutrinos of TXS 0506+056 in an environment where dominantly Compton scattering supports the pair cascading, appears feasible. Eq. 24 and Eq. 23 imply in this case still very inefficient neutrino production, and a corresponding pair cascade flux that lies significantly below the gamma-ray flux level observed by the LAT during the neutrino flare (see Figs. 6-10). Further high energy radiation processes are therefore needed to explain the observed gamma-ray SED, which is unlikely protoninitiated, during the neutrino flare.

5. DISCUSSION AND CONCLUSIONS

In this work we present a procedure to derive constraints on the broadband photon spectral energy distribution for a given (observed) neutrino spectrum and in the framework of photo-hadronically produced neutrinos from relativistic protons accelerated in jetted AGN. This

| Origin of target photon field | Further setup constraints | Results |
|--------------------------------|---------------------------|--|
| All target photon fields | $u_t' \gg u_B'$ | no constraints |
| (cascading constraints) | $u_t' \le u_B'$ | $\tau_{\gamma\gamma,\text{max}} \sim \text{(a few) } 10 \text{ for } D \leq 10$ $\tau_{\gamma\gamma,\text{max}} \sim \text{(a few) } 10^{12} \text{ for } D \gg 10$ |
| | | $\tau_{\gamma\gamma,\text{max}} \sim \text{(a few) } 10^{12} \text{ for } D \gg 10$ |
| Co-moving target photon field | | ruled out: too high L_p (Eq. 15); |
| | | p syn overshoots X-ray archival flux (Eq. 18,19) |
| Stationary target photon field | $u_t' \le u_B'$ | ruled out: target photon flux overshoots UV/ |
| | | soft X-ray archival flux (Eq. 21) |
| | $u_t' \gg u_B'$ | viable: target photon flux below UV/ |
| | | soft X-ray archival flux (Eq. 20); |
| | | L_p (Eq. 26) acceptable for sufficiently large D |

 $[^]a {\it Includes}$ cascading constraints.

Table 1. Summary of tested setups and results.

procedure can accommodate any origin for the dominant target photon field. For this purpose we first reconstruct, in the co-moving jet-frame, the minimum target photon spectrum required to produce the neutrino spectrum, and calculate all corresponding further secondary particles produced through these interactions (photomeson and Bethe-Heitler pair production). A rather narrow energy range at hard X-rays (in the co-moving jet frame) is sufficient to explain the 2014/15 IceCube neutrino flare spectrum from the direction of TXS 0506+056 by photomeson production of relativistic protons from an injection spectrum with index $\alpha_p = 2.0 \pm 0.1 2$ extending to PeV – hundreds of PeV energies. For typical spatial scales of the emission region and magnetic field strengths these protons are well contained in this region.

The produced high-energy photons and electronpositron pairs initiate electromagnetic cascades in the neutrino emission region with an efficiency that is directly linked to the neutrino production rate. Both the energy-dependent pair production optical depth and the radiation process (inverse Compton scattering, synchrotron radiation) that feed the cascades determine the resulting shape of the photon spectrum escaping the source. The so derived photon spectrum, for a given Doppler factor, can be considered as the minimum radiation emerging from the source that is strictly associated with the photo-hadronically produced neutrinos. By comparing our simulated cascade spectra to broadband SEDs from observations carried out quasisimultaneous to the neutrino detection, one can then derive constraints on the environment of the neutrinoproducing site. A summary of the tested setups and resulting constraints is provided in Tab. 1.

A comprehensive study of these (steady-state) minimum cascade SEDs, when operating in a narrow X-ray target photon field, reveals rather low flux levels at GeV-energies if inverse Compton radiation feeds the cascade, even for an optically thin radiative environment. In case of highly magnetized environments where pair synchrotron losses can not be neglected, the synchrotron/Compton-synchrotron supported cascades extend across a much wider energy range than the Compton-supported cascades, down to radio/optical frequencies. This allows deep optical to X-ray measurements to set limits on the efficiency of neutrino production in this region.

The efficient photo-pion production of \sim PeV neutrinos requires a high target-photon density, leading to $\gamma\gamma$ absorption depths $\tau_{\gamma\gamma}\gg 1$ for \sim GeV photons. We therefore concluded that efficient photo-pion production of IceCube neutrinos in blazars does not predict a causal

connection between quasi-contemporaneous GeV γ -ray and neutrino emission here.

We then combined the derived limits on the $\gamma\gamma$ opacity from the cascade SEDs and co-moving neutrino luminosity of TXS 0506+056 with direct observational constraints from its MWL SED in the expected energy range of the required minimum target photon field. Considering first the extreme case of a co-spatially produced (co-moving) target photon field for photo-pion production of the neutrino flare of TXS 0506+056, we deduced extreme values for the required proton kinetic power and a too high proton synchrotron component that would violate the observed photon SED at X-ray energies. This makes such a scenario implausible. Also regarding the case of a stationary (in the AGN frame) target photon field as the other extreme case results in too high expected flux values in the soft X-ray regime as compared to the observed SED if synchrotron or Comptonsynchrotron cascades operate in the neutrino emission region.

The only viable scenario appears to be a stationary soft X-ray photon field providing the targets for photopion production of the observed neutrinos with the resulting cascades being fed by inverse Compton radiation only. The required proton kinetic powers appear in a plausible range for a jet powered by accretion onto a supermassive black hole, and the expected proton synchrotron component does not exceed the observed X-ray flux for not too large field strengths. In this environment, however, neutrino production is very inefficient $(\tau_{p\gamma} \sim 10^{-3} \text{ for typical blazar model parameters})$ during the neutrino flare and the associated pair cascade GeV-flux too low to explain the LAT observations. The origin of the LAT spectrum observed during the neutrino flare period can therefore not be associated with the neutrino producing mechanism, and the GeV-flux has to be emitted from zones in the jet other than the neutrino zone. Any link between the neutrino and GeVflux is then determined by a corresponding connection between the γ -ray and neutrino emitting zones.

The work of M.B. is supported through the South African Research Chair Initiative of the National Research Foundation⁸ and the Department of Science and Technology of South Africa, under SARChI Chair grant No. 64789. A.R. acknowledges financial support from the Austrian Science Fund (FWF), project I 3452-N27.

⁸ Any opinion, finding and conclusion or recommendation expressed in this material is that of the authors and the NRF does not accept any liability in this regard.

SB was supported by the NASA Postdoctoral Program.

We are grateful to Valentina La Parola, Alberto Segreto and Marco Ajello for being instrumental in deriving the *BAT* upper limit used in this work. We also thank Matthew Baring for providing valuable comments that lead to significant improvements of the manuscript, and P. Padovani and A. Tohuvavohu for valuable discussions on the manuscript text. We also thank K. Murase who pointed out to us the work Murase et al (2018), and S. Gao who pointed out to us the work Gao et al (2017).

We thank the ASAS-SN team for providing publicly, real time optical data used in this work.

The Fermi-LAT Collaboration acknowledges generous ongoing support from a number of agencies and institutes that have supported both the development and the operation of the LAT as well as scientific data analysis. These include the National Aeronautics and Space Administration and the Department of Energy in

the United States, the Commissariat à l'Energie Atomique and the Centre National de la Recherche Scientifique / Institut National de Physique Nucléaire et de Physique des Particules in France, the Agenzia Spaziale Italiana and the Istituto Nazionale di Fisica Nucleare in Italy, the Ministry of Education, Culture, Sports, Science and Technology (MEXT), High Energy Accelerator Research Organization (KEK) and Japan Aerospace Exploration Agency (JAXA) in Japan, and the K. A. Wallenberg Foundation, the Swedish Research Council and the Swedish National Space Board in Sweden.

Additional support for science analysis during the operations phase is gratefully acknowledged from the Istituto Nazionale di Astrofisica in Italy and the Centre National d'Études Spatiales in France. This work performed in part under DOE Contract DE-AC02-76SF00515.

Software: Fermipy (v0.17.3, Wood et al. 2017), batimager (Segreto et al. 2010), SOPHIA (Mücke et al. 2000), Protheroe & Johnson (1996)

REFERENCES

Aartsen, M.G., et al. [IceCube Collaboration], 2013, Science, 342,1242856

Aartsen, M.G., et al. [IceCube Collaboration], 2014, Physical Review Letters 113, 101101

Aartsen, M.G., et al. [IceCube Collaboration], 2015, ApJ809, 98

Aartsen, M.G., et al. [IceCube Collaboration], 2018, Science 361, eaat1378

Aartsen, M.G., et al. [IceCube Collaboration], 2018, Science 361, 147-151

Abeysekara, A.U.., et al. [VERITAS Collaboration], 2018, ApJ 861, 20

Acero, F., et al. [Fermi-LAT Collaboration], 2015, ApJS 218, 23

Ackermann, M., et al. [Fermi-LAT Collaboration], 2016, ApJS 222, 5

Aharonian, F., 2000, New Astronomy, 5, 377

Ansoldi, S., et al. [MAGIC Collaboration], 2018, ApJL 863, L10

Ajello, M., Romani, R. W., Gasparrini, et al. 2014, ApJ, 780, 73

Atoyan, A., Dermer, C.D., 2001, Phys. Rev. Lett, 87, 1102 Atoyan, A., Dermer, C.D., 2003, ApJ, 586, 79

Bednarek, W., Protheroe, R. J., 1997, MNRAS, 287, 9

Bednarek, W., Protheroe, R. J., 1999, MNRAS, 302, 373

Begelman, M. C., Rudak, B., Sikora, M., 1990, ApJ, 362, 38

Begelman, M. C., Fabian, A. C., & Rees, M. J. 2008, MNRAS, 384, L19 Böttcher, M., Mause, H., & Schlickeiser, R., 1997, A&A, 324, 395

Böttcher, M., Reimer, A., Sweeney, K. & Prakash, A. 2013, ApJ, 768, 54

Cerruti, M., Zech, A., Boisson, C., & Inoue, S., 2015, MNRAS, 448, 910

Dermer, C.D., Schlickeiser, R., 1993, ApJ, 416, 458

Dermer, C. D., Ramirez-Ruiz, E., & Le, T., 2007, ApJ, 664, L67

Dermer, C. D., Razzaque, S., Finke, J. D., Atoyan, A., New Journal of Physics, 11, 065016

Dermer, C.D., Murase, K., Takami, H., 2012, ApJ, 755, 20

Dermer, C.D., Murase, K., Inoue, Y., 2014, Journal of High-Energy Astrophysics, 3, 29

Dimitrakoudis, S., Mastichiadis, A., Protheroe, R. J., Reimer, A., 2012, A&A, 546, 120

Dimitrakoudis, S., Petropoulou, M., & Mastichiadis, A., 2014, Astropart. Phys., 54, 61

Franceschini, A. & Rodighiero, G., 2017, A&A, 603, A34

Gao, S. and Pohl, M. and Winter, W. 2017, A&A, 603, A34

Garrappa, F., Buson, S., Franckowiak, A., ASAS-SN and IceCube collaboration 2018, submitted

Hillas, M., 1984, ARA&A, 22, 425

Halzen, F., 2013, Astroparticle Physics, 43, 155

Kadler, M., Krauss, F., Mannheim, K., et al., 2016, Nature Physics, 12, 807

Kochanek, C. S., Shappee, B. J., Stanek, K. Z., et al. 2017, PASP, 129, 104502

- Krauss, F., Kadler, M., Mannheim, K., et al., 2014, A&A, 440, 775
- Kelner, S. R., & Aharonian, F. A., 2008, Phys. Rev. D, 78, 034013
- Mannheim, K., Biermann P.L., 1989, A&A, 221, 211
- Mannheim, K., Stanev, T., Biermann, P. L., 1992, A&A, 260, 1
- Mannheim, K., 1993, A&A, 269, 67
- Mannheim, K. & Schlickeiser, R., 1994, A&A, 286, 983
- Mannheim, K., Protheroe, R. J., Rachen, J. P., Phys. Rev. D, 63, 3003
- Mastichiadis, A., 1996, Space Science Reviews, 75, 317
- Mücke, A., Rachen, J.P., Engel, R., Protheroe, R.J., Stanev, T., 2000, Nuclear Physics B Proceedings Supplements, Vol. 80; arXiv:astro-ph/9905153
- Mücke, A., Engel, R., Rachen, J. P., Protheroe, R.J., Stanev, T., 2000, CPC, 124, 290
- Mücke, A., Protheroe, R. J., 2000, AIP Conference Proceedings, 515, 149-153
- Mücke, A., Protheroe, R. J., 2001, Astroparticle Physics, 15, 121
- Mücke, A., Protheroe, R. J., Engel, R., Rachen, J. P., Stanev, T., 2003, Astroparticle Physics, 18, 593
- Murase, K., Inoue, Y., Dermer, C.D., 2014, Phys. Rev. D, 90, 3007
- Murase, K., Guetta, D., & Ahlers, M., 2016, Phys. Rev. Lett., 116, 071101
- Murase, K., Oikonomou, F., Petropoulou, M. 2018 ApJ, 865, 124
- Osterbrock, D.E., Ferland, G.J., 2006, Astrophysics of Gaseous Nebulae and Active Galactic Nuclei, University Science Books, Sausalito, California
- Padovani, P., Petropoulou, M., Giommi, P., & Resconi, E., 2015, MNRAS, 452, 1877

- Padovani, P., Giommi, P. and Resconi, E. et al, 2018, MNRAS, 480, 192
- Padovani, P., Oikonomou, F., Petropoulou, M., Giommi, P. and Resconi, E. et al, 2019, MNRAS, 484, 104
- Paiano, S., Falomo, R., Treves, A., & Scarpa, R., 2018, ApJ, 854, L32
- Pacholczyk, A. G., 1970. Radio Astrophysics, W. H. Freeman and Company, San Francisco.
- Petropoulou, M., Dimitrakoudis, S., Padovani, P., Mastichiadis, A., & Resconi, E., 2015, MNRAS, 448, 2412 Protheroe, R.J., 1990, MNRAS, 246, 628
- Protheroe, R.J., Mastichiadis, A. & Dermer, C.D., 1992, Astroparticle Physics, 1, 113
- Protheroe, R. J., Szabo, A. P., 1992, Phys. Rev. Lett, 69, 2885
- Protheroe, R.J. & Stanev, T., 1993, MNRAS, 264, 191
- Protheroe, R.J. & Johnson, P.A., 1996, Astroparticle Physics, 4, 253
- Protheroe, R.J., 1999, Nucl. Phys. B Suppl., 77, 465
- Protheroe, R. J., Donea, A.-C., Reimer, A., 2003, Astroparticle Physics, 19, 559
- Reimer, A., Protheroe, R. J., Donea, A.-C., 2004, A&A, 419, 89
- Reimer, A. & Böttcher, M., 2013, Astroparticle Physics, 43, 103
- Roustazadeh, P. & Böttcher, M. 2010, ApJ, 717, 469
 Segreto, A., Cusumano, G., Ferrigno, C., et al. 2010, A&A, 510, 47
- Shappee, B. J., Prieto, J. L., Grupe, D., et al. 2014, ApJ, 788, 48
- Sitarek, J. & Bednarek, W., 2012, MNRAS, 421, 512
- Stecker, F. W., Done, C., Salamon, M. H., Sommers, P., 1991, Phys. Rev. Lett., 66, 2697
- Svensson, R., 1987, MNRAS, 227, 403
- Szabo, A. P., Protheroe, R. J., 1994, Astroparticle Physics, 2, 375
- Wood, M. et al 2017, ICRC, 35, 824